Heliyon 9 (2023) e17426

Contents lists available at ScienceDirect

Heliyon

journal homepage: www.cell.com/heliyon

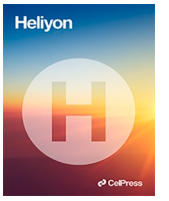

Solar-driven CO_2 reduction using modified earth-abundant ilmenite catalysts

E. Luévano-Hipólito [a,b], Mayte G. Fabela-Cedillo [b], Leticia M. Torres-Martínez [b,c,*], María E. Zarazúa-Morín [b]

[a] *CONACYT - Universidad Autónoma de Nuevo León, Facultad de Ingeniería Civil-Departamento de Ecomateriales y Energía, Cd. Universitaria, C.P. 66455, San Nicolás de los Garza, NL, Mexico*

[b] *Universidad Autónoma de Nuevo León, Facultad de Ingeniería Civil-Departamento de Ecomateriales y Energía, Cd. Universitaria, C.P. 66455, San Nicolás de los Garza, NL, Mexico*

[c] *Centro de Investigación en Materiales Avanzados, S. C. (CIMAV), Miguel de Cervantes 120 Complejo Ind. Chihuahua, Chihuahua, Chih, 31136, Mexico*

ARTICLE INFO

Keywords:
CO_2 reduction
$NaFeTiO_4$
Earth-abundant materials
Ilmenite
Solar-driven reaction
Formic acid

ABSTRACT

Photocatalytic CO_2 reduction is an alternative technology to the depletion of highly pollutant fossil fuels through the generation of renewable solar-based fuels. This technology requires that the photocatalysts be obtained directly from nature to scale up the process. Taking that into consideration, this work proposed the fabrication of sodium iron titanate ($NaFeTiO_4$) photocatalysts from earth-abundant ilmenite mineral. The photocatalysts exhibited full spectrum light response, good electron transfer due to its unique tunnel structure that favored the formation of rod-like morphology. These properties promoted the solar-driven CO_2 reduction to generate formic acid (HCOOH) with high selectivity (157 μmol g^{-1} h^{-1}). It was found that higher synthesis temperatures promoted the formation of Fe^{3+} species, which decreased the efficiency for CO_2 reduction. Also, the possibility of reduced the CO_2 molecules in the air was studied with the $NaFeTiO_4$ samples, which resulted in an efficiency of up to 93 μmol g^{-1} h^{-1} of HCOOH under visible light. The stability of the solar-driven CO_2 reduction with the $NaFeTiO_4$ photocatalysts was confirmed after seven days of continuous evaluation.

1. Introduction

The photocatalytic CO_2 reduction reaction (CO2RR) is a promising approach to generating clean and renewable solar fuels from earth-abundant sources, e.g., CO_2, H_2O, photocatalysts, and solar light. However, to scale up this process, it is necessary to obtain the photocatalysts directly from nature (e.g., minerals) without using complicated, toxic, and expensive reactants [1]. So far, there are a limited number of reports about using minerals directly as a photocatalyst or as support for CO2RR [2–8]. In these works, the use of earth-abundant materials has promoted better efficiencies than bare semiconductors for CO_2 reduction to generate various solar fuels such as HCOOH, HCOH, CH_3OH, CO, and CH_4, as is shown in Table 1. The reason behind of this boost in the activity has been related to several factors, e.g., high surface area, full spectrum light response, good conductivity, and they prevent the agglomeration of the

* Corresponding author. Universidad Autónoma de Nuevo León, Facultad de Ingeniería Civil-Departamento de Ecomateriales y Energía, Cd. Universitaria, C.P. 66455, San Nicolás de los Garza, NL, Mexico.

E-mail address: lettorresg@yahoo.com (L.M. Torres-Martínez).

https://doi.org/10.1016/j.heliyon.2023.e17426
Received 19 February 2023; Received in revised form 13 June 2023; Accepted 16 June 2023
Available online 19 June 2023

photocatalyst, thus a higher number of active sites are available for the CO2RR.

Ilmenite ($FeTiO_3$) is one of the most studied earth-abundant minerals for various photocatalytic reactions [9–13]. Although ilmenite ore has been commonly used as a raw material to produce TiO_2, several studies have demonstrated its photocatalytic activity to degrade different dyes, and its antibacterial activity has been recently revealed under light and dark conditions [12,13]. However, its use for the photocatalytic CO2RR has not been explored; only Truong et al. reported the photocatalytic activity of synthetic $FeTiO_3/TiO_2$ composite for methanol generation (0.5 μmol g^{-1} h^{-1}) from CO2RR under UV and visible light [14].

The application of ilmenite as a photocatalyst has been limited since the natural ore consists of various impurity elements (e.g., Fe, Mn, V, C) and complicated crystal lattice defects, which affect its photocatalytic performance [15–17]. As an alternative to the direct use of ilmenite, several authors have proposed obtaining new phases using the ore mineral as raw material, e.g., TiO_2 (anatase and rutile), $K_4Ti_3O_8$, Fe_2TiO_5, TiP_2O_7, TiC, Fe_2O_3, $Fe_2Ti_3O_9$, and $NaFeTiO_4$ [18–25]. Among them, the sodium iron titanate phase ($NaFeTiO_4$) is of high interest in photocatalysis due to its tunnel structure, in which the octahedra share an edge at one level in linear groups of three, giving a vast space for the three octahedra. It has been reported that the presence of the tunnel structure in a photocatalyst distorts TiO_6 closely and it promoted an efficient production of photoexcited charges [26]. Thus, its use as a photocatalyst in the CO2RR is highly interesting. Also, $NaFeTiO_4$ has demonstrated to be a suitable adsorbent for Cu^{+2}, Cd^{+2}, and Pb^{+2} ions [25], and recently its photocatalytic activity was demonstrated to remove rhodamine and methylene blue dyes from wastewater and evolute hydrogen from water splitting due to its favorable flat band potential (−0.101 V *vs.* Ag/AgCl, 0.1 M KCl) [27]. Considering this, here is proposed the synthesis of $NaFeTiO_4$ by using ilmenite ore as a low-cost raw material with photocatalytic activity under visible and solar light irradiation to generate various solar fuels, e.g., HCOOH, HCOH, and CH_3OH. Also, the CO_2 used as raw material was desorbed from previously (and naturally) captured in igneous rocks, dolomite. In summary, this work proposed the conversion and utilization of captured CO_2 using earth-abundant materials using solar light as a driven force.

Table 1
Summary of reports about using minerals as photocatalyst in the CO2RR.

Photocatalyst (Mineral)	Solar fuel (μmol g^{-1} h-1)	Light source	Reaction conditions	Contribution	Ref.
ZnS/$CuFeS_2$/ZnO (Sphalerite)	HCOOH (1693)	Visible lamp, 400–700 nm (LED 20 W)	· Batch reactor. · 0.13 atm. · 25 °C. · 0.01 g catalyst. · H_2O	· Traces of $CuFeS_2$ allowed the visible-light response of hierarchical ZnS/ZnO.	2
$Cu_2O/Mg(OH)_2$ (Dolomite)	HCOH (419) CH_3OH (11)	Visible lamp, 400–700 nm (LED 20 W)	· Batch reactor. · 0.13 atm. · 25 °C. · 0.1 g catalyst. · H_2O	· Dolomite provided Ca^{2+} and Mg^{2+} active sites with high surface area for CO_2 adsorption and a better charge transfer between the components.	3
TiO_2/Kaolinite (Kaolinite)	CH_4 (0.3) CH_3OH (0.2)	UV lamp, 254 nm (8 W)	· Batch reactor. · 1 atm. · 25 °C · 1 g L^{-1} catalyst. · 0.2 M NaOH	· Kaolinite changes the acid-basic properties of the photocatalyst, inhibit the recombination of the electron and hole and prevent the formation of aggregates in suspension.	4
MoO_{3-x}/H-Pal (Palygorskite)	CH_3OH (6.2)	Visible lamp (300 W)	· Batch reactor. · 25 °C. · 0.1 g catalyst. · H_2O	· The presence of abundant hydroxyl groups on Pal favors the growth or assembly of active species.	5
CeO_2/ATP (Attapulgite)	CO (309) CH_4 (184)	UV lamp, 254 nm (8 W)	· Batch reactor. · 1 atm. · 0.05 g catalyst. · 0.1 M NaOH/ 1.2 M CH_3CN	· ATP improves the CO2RR efficiency due to its high conductivity, which promoted electron transport and enhanced the separation efficiency of the electron holes.	6
WO_3/Bt/g-C_3N_4 (Bentonite)	CO (160) CH_4 (560)	Visible lamp, (35 W)	· Gas-phase reactor. · 0.05–0.25 g catalyst. · H_2O	· The introduction of BT in the photocatalyst modified the selectivity from CO to CH_4 generation and it acts as electron moderator.	7
Cu/Silica rocks (Silica)[a]	HCOOH (0.05)	Sunlight	· Batch reactor. · 1 atm. · 25 °C.	· 30% Cu-loaded quartzdiorite favored the highest HCOOH formation under sunlight.	8
$FeTiO_3/Fe_2O_3$ $NaFeTiO_4$/ Fe_3O_4 (Ilmenite)	*This work reports the use of earth-abundant mineral to fabricate novel photocatalyst with tunnel structure with solar activity to generate HCOOH.*				

[a] Silica rocks refers to a group of Amphibolite, gneiss, granite, granodiorite, phyllite, quartzdiorite, and shale.

2. Methodology

2.1. Materials

For the synthesis, ilmenite mineral was donated by a local Steel Factory. The mineral was washed with distilled water and ground in a ball mill to ensure its homogenization. Then, it was subjected to a thermal treatment at 800, 900, and 1000 °C at 10 °C min^{-1} as a reference. These samples were identified as IL*x*, where *x* represents the calcination temperature.

In addition, the grounded ilmenite (0.0067 mol of $FeTiO_3$) was mixed with stoichiometric amounts of Na_2CO_3 (DEQ, 99%) in an agate mortar, according to **equation (1)**. The mixture was annealed at different temperatures (800, 900, and 1000 °C), which were identified as NFTO-*x*, where *x* represents the calcination temperature.

$$2\,FeTiO_3 + 3\,Fe_2O_3 + Na_2CO_3 \rightarrow^{\Delta} 2\,NaFeTiO_4 + 2\,Fe_3O_4 + CO_2\uparrow \quad (1)$$

2.2. Characterization of the materials

The thermal behaviour of the mineral and the NFTO precursor was investigated by a thermogravimetric (TGA) and Differential Thermal Analysis (DTA) in a LINSEIS model STA PT 1600. The crystal phases of the pristine and modified mineral were identified by X-ray diffraction (XRD) in a Bruker D8 Advance diffractometer from 10° to 70° and a step size of 0.02° using Cu-Kα radiation. Scanning electron microscopy (SEM) was used to determine the morphology of the samples using a JEOL microscope JSM-6490LV equipped with an Oxford energy dispersive detector (EDS). UV–Visible (UV–Vis) spectroscopy was used to calculate the bandgap energy of the minerals in a spectrophotometer model Cary 5000, Agilent Technologies. The absorption spectra were converted with the remission function of Kubelka-Munk (K-M) to calculate the band gap energy of the materials. Photoluminescence spectra of the samples were obtained in a Cary Eclipse spectrophotometer using an excitation wavelength of 450 nm. The Brunauer-Emmett-Teller (BET) method was used to determine the specific surface area of the materials by means of N_2 adsorption-desorption measurements using a Quantachrome Nova 2000e Instruments. The isotherms were evaluated at −196 °C after a sample pre-treatment at 250 °C during 3 h. Electrochemical impedance spectroscopy (EIS) was conducted in an electrochemical workstation with a standard three-electrode cell model Autolab PGSTAT 302 N. The working electrode used has an area of 1 cm^2, with Pt bar as a counter electrode, and Ag/AgCl as a reference electrode using 0.5 M of NaOH as the electrolyte.

2.3. CO_2 photoreduction tests

The photocatalytic experiments were performed in a semi-batch reactor with a continuous flow of CO_2 (1 L min^{-1}). In each experiment, 0.05 g of catalyst was dispersed in 100 mL of distilled water. Three different scenarios were used to evaluate the activity of the catalyst:

i) Air was directly used as CO_2 source using a LED lamp that emit in the visible region (400–700 nm) at room and pressure conditions. The flow rate was maintained at 3 L min^{-1}.
ii) Dolomite was used as a CO_2 precursor for the experiments using a LED lamp. The dolomite reacted with acetic acid (5% v/v) to generate a pure flow of CO_2 that was conducted to photocatalytic reactor at the same volumetric flow than the first scenario. The properties of the dolomite used was previously reported [3].
iii) In this case, CO_2 was generated from the dolomite (as ii), but in this scenaroi the reactor was exposed to direct solar irradiation. The experiments were performed at 13:00 horas since there is the highest irradiance of the day. For reference the irradiance evolution during the day is shown in Fig. S1. The suspension into the reactor was magnetically stirring, using two magnets behind the reactor controlled by a fan powered by a commercial solar cell. The set-up used for these experiments is schematized in Scheme 1.

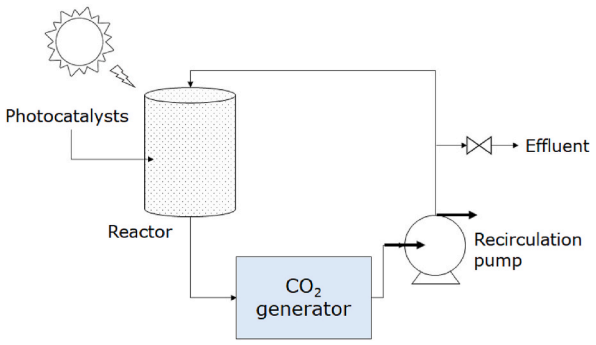

Scheme 1. Schematic set-up for the solar-driven photocatalytic experiments.

Analysis of variance (ANOVA) was used to identify if the differences in the CO_2 reduction efficiencies observed among the studied samples were statistically significant using the Minitab® software version 19. For this purpose, each scenario was considered as a block to analyze the experiments.

3. Characterization results

The thermal analyses of the ilmenite ore were performed to evaluate the influence of temperature on the material mass loss and other possible transitions. Fig. 1a shows the thermal behavior of the ilmenite ore previously washed and homogenized. The loss of mass at temperatures lower than 200 °C is related to the endothermic evaporation of the remaining water. The main mass loss occurred after 400 °C, which could be related to the oxidation of $Fe_2O_3 \rightarrow Fe_3O_4$ [28]. Also, the thermal behavior of the NFTO precursor is shown in Fig. 1b. Again, it was observed a small weight loss at temperatures lower than 200 °C, related to the evaporation of water or other volatile compounds. A similar comportment was observed from 500 °C, related to the oxidation of iron oxide. However, the crystallization of the $NaFeTiO_4$ compound was observed around 850 °C, which is agreement with previous reports [29,30].

The analysis of the X-ray diffraction pattern showed that the main phases found in the ilmenite ore are $FeTiO_3$ (JCPDS 75–0519) and Fe_2O_3 (JCPDS 33–0664), as shown in Fig. S2. In addition, other minor phases, such as quartz SiO_2 (JCPDS 46–1045), spinel $MgAl_2O_4$ (JCPDS 21–1152), and rutile TiO_2 (JCPDS 21–1276) were identified.

Fig. 2 shows the XRD patterns of the NFTO samples annealed at different temperatures. The sample obtained at 800 °C shows the $NaFeTiO_4$ phase (JCPDS 33–1255) as the primary contributor, with secondary phases such as Fe_2O_3, Fe_3O_4, and SiO_2. The presence of an amorphous phase was identified at higher temperatures, which could favor the densification and grain growth of the NFTO samples.

The surface morphology of the synthesized samples and the ilmenite ore was investigated by SEM. As shown in Fig. 3a, the ilmenite ore exhibited a heterogenous morphology composed of micrometer particles (100–200 μm). On the other hand, the NFTO samples exhibited different morphology. As soon as the $NaFeTiO_4$ appeared, rod-like particles were formed (Fig. 3b). These rods continue to grow as the temperature increases, as is shown in Fig. 3c and d. The rods were covered by iron oxide particles in some parts of the sample (Fig. 3e), which agrees with the XRD results. Additionally, EDS analysis revealed that the global elemental composition of the samples was composed of Na, Fe, Ti, and O, as is depicted in Fig. 3f.

Fig. 4 represents the K-M spectra versus the photon energy for the reference and the synthesized samples. The pristine mineral absorbs in a wide interval of the UV–Visible spectra, in which the band edge was not visibly observed; meanwhile, the NFTO samples exhibited a different behavior. The absorption edge of the NFTO samples shifts to lower photon energy upon increasing the annealed temperatures. As a result, the band gap energies of the samples were 1.9 eV (NFTO-800), 1.8 eV (NFTO-900), and 1.7 eV (NFTO-1000 °C) (Table 2). Previous work reported that the band gap energy of $NaFeTiO_4$ synthesized from pure reactants was 1.75 eV [27], suggesting that the iron oxide impurities did not significantly influence modifying the band energy of the NFTO samples.

Fig. 5 plots the PL spectra of the reference and the as-prepared NFTO samples excited at 450 nm. The NFTO samples exhibited a higher PL intensity than the reference sample, probably because of their different composition. These samples showed a broad emission, which was deconvoluted to investigate the possible different emissions in the NFTO samples. The *input* image of Fig. 5 shows that the PL spectrum was deconvoluted into three different emissions centered at 675 (1), 715 (2), and 750 nm (3). Despite there are not enough reports of the photoluminescence of $NaFeTiO_4$, recently, Shendi et al. reported its emission around 600 nm [27]; however, the origin of this emission still needs to be determined. Nevertheless, this data could suggest that the first emission observed could be related to the $NaFeTiO_4$ since the reference sample did not show this band. In addition, the second and third emissions have been

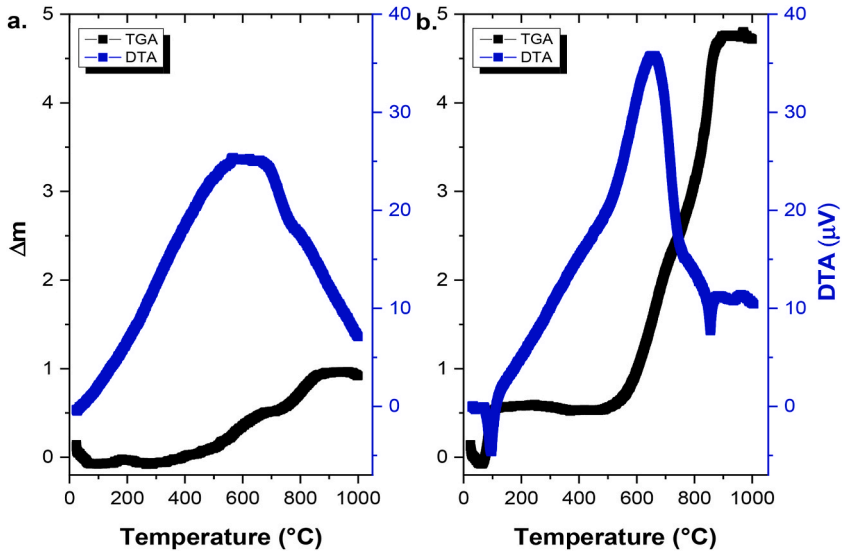

Fig. 1. Simultaneous TGA/DTA curves of a. ilmenite ore and b. the NFTO precursor.

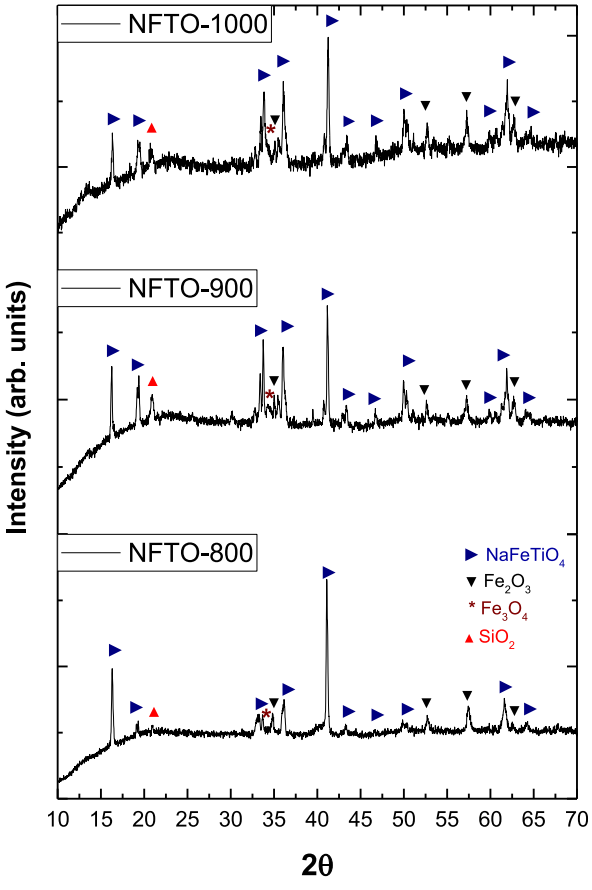

Fig. 2. XRD patterns of the NFTO samples.

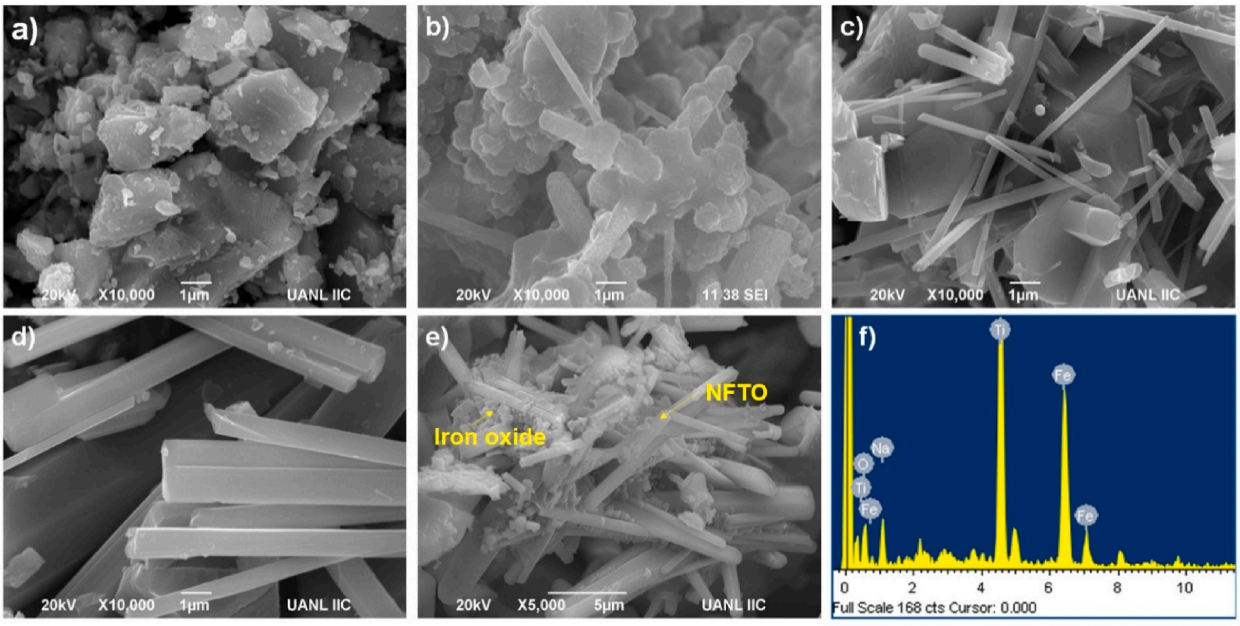

Fig. 3. SEM images of the samples: a. Ilmenite ore, b. NFTO-800, c. NFTO-900, d-e. NFTO-1000, and f. EDS of NFTO-1000.

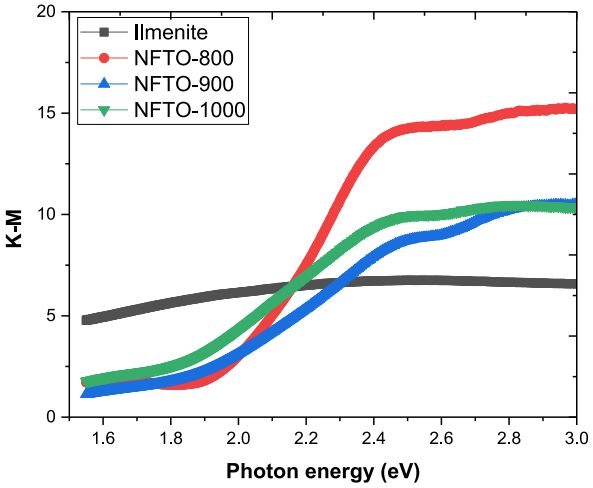

Fig. 4. K-M spectra of the reference and NFTO synthesized samples.

Table 2
Surface area and band gap of the reference and as-prepared samples.

Sample	Surface area ($m^2\ g^{-1}$)	Band gap (eV)
Ilmenite	<1	–
NFTO-800	8.3	1.9
NFTO-900	2.3	1.8
NFTO-1000	<1	1.7

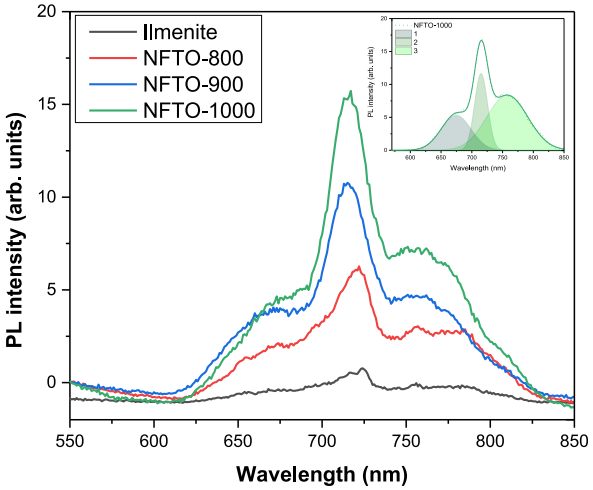

Fig. 5. Photoluminescence (PL) spectra of the reference and NFTO samples. *Input*: Deconvoluted spectra of the NFTO-1000 sample.

associated with the near-infrared region of Fe_2O_3 and the transitions from different Fe^{3+} sites [31,32]. Particularly, these bands were more prominent in the NFTO samples annealed at higher temperatures (900 and 1000 °C).

The BET analysis showed that the samples exhibited low surface area values. The tabulated surface area values for the NFTO samples indicated that upon increasing the temperature, these values tended to lower values, as expected since higher temperatures promoted the agglomeration of the particles in order to decrease their surface energy. The NFTO sample exhibited a slightly higher surface area value (8.3 $m^2\ g^{-1}$) among the studied samples with a pore volume of around 0.029 $cm^3\ g^{-1}$. N_2 isotherms of the synthesized NFTO samples are shown in Fig. S3. The profile of the isotherms is related to type IV hysteresis, in which a narrow area in the lower-pressure region indicates an open porous structure, and the presence of macropores is indicated by the hysteresis loop at the high-pressure region [33].

Electrochemical impedance spectroscopy measurements were performed to examine the charge transfer resistance of the reference

and the synthesized samples. Fig. 6a shows the Nyquist plot of the studied samples; in this context, the semicircle diameter indicates the carrier transfer resistance. As shown, the corresponding arc radius of the NFTO samples decreased in the samples synthesized at lower synthesis temperatures, indicating a lower impedance in the NFTO-800 sample. The reference mineral exhibited a small arc radius, probably related to an accumulated charge at the electrode-electrolyte interface. However, the charge transfer is not favored in the reference mineral since it lacks enough surface area, homogeneous morphology, or particle size, as it will be further discussed.

In addition, the Bode phase plots of the samples are shown in Fig. 6b. Although the $NaFeTiO_4$ samples exhibited similar behavior, a slight shift was observed towards the high-frequency region, suggesting a more efficient and fast electron transfer in the NFTO-800 sample. On the contrary, the reference exhibited a lower electron transfer compared than the $NaFeTiO_4$ samples. These results agree with the PL results, which could suggest that a higher presence of Fe^{3+} species decreases the efficiency of the charge transfer.

4. CO_2 reduction

The photocatalytic activities of the ilmenite mineral (as reference) and the $NaFeTiO_4$ samples were evaluated in the CO_2 reduction under different scenarios. First, it was studied the possibility of reducing the CO_2 present in the air in an indoor place, which generally has a higher CO_2 concentration than the outdoors [34]. The efficiency of the CO_2 reduction directly from the air was quantify through the formation of formic acid. In these experiments, the samples were activated with a visible LED lamp that emits from 400 to 700 nm and the CO_2 concentration in the room was 450 $\pm$ 10 ppm.

As shown in Fig. 7, the NFTO samples exhibited similar behavior to generate formic acid directly from the air under visible light. In this case, 93, 90, and 73 μmol of HCOOH were detected per gram of the NFTO-800, NFTO-900, and NFTO-1000 photocatalysts, respectively. These efficiencies were much higher than the ilmenite sample, which formed less than 1 μmol of the product per gram.

In addition, the samples were evaluated using a higher concentrate CO_2 stream under the same irradiation source. Under this scenario, higher HCOOH yields were obtained probably because of the higher CO_2 concentration in the stream. In this case, the highest efficiency to generate HCOOH was 155 μmol g^{-1} h^{-1}, which was obtained with the NFTO-800 sample. However, according to the ANOVA results, the efficiencies were very closed among the studied samples, and which differences were not significant (Table S1).

The third scenario offers the possibility of study the photocatalytic activity of the proposed materials under real conditions. In this case, the samples were evaluated using a continuous flow of CO_2 under direct solar light exposure (average irradiance ~650 W m^{-2}). As a result, a pronounced increase of the formic acid was observed in the three $NaFeTiO_4$ samples. Here, the differences observed in the yield obtained among the samples were significant, as is shown in Table S1.

From these results, it was confirmed that the NFTO-800 sample exhibited the best activity of the studied samples. This could be associated with its higher crystallinity since the rest of the samples showed an amorphous phase that did not contribute positively to the charge transfer required, probably due to the crystal imperfections [35]. Also, another factor that could influenced the photocatalytic efficiency of the samples is the presence of the Fe^{3+} species. PL analysis evidenced the higher contribution of the Fe^{3+} species in the samples annealed at higher temperatures, these species could act as electron scavenger since the potential of the Fe^{+3}/Fe^{2+} couple is 0.77 *vs*. NHE [36], which is more positive than the conduction band potential of the $NaFeTiO_4$ photocatalyst [27]. Also, Fe^{3+} species significantly favored the chemisorption of CO_2, which limits the gas desorption and consequently, the reaction yield [37]. Considering this, the NFTO-800 sample was selected for the stability analysis.

To investigate the origin of the products obtained, four different blank experiments were performed. As is shown in Fig. S4, the CO_2 photolysis and the NFTO-800 sample evaluated under dark conditions did not produce any amount of HCOOH from the photocatalytic CO_2 reduction. Also, this sample was evaluated under a CO_2 atmosphere at dark conditions. After 1 h, the sample produced <2 μmol,

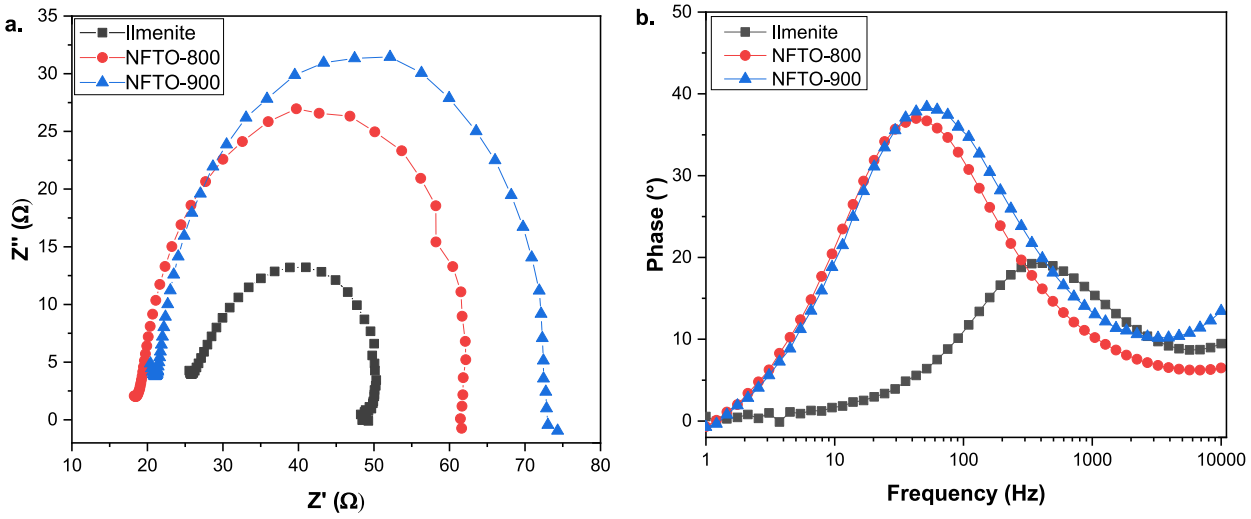

Fig. 6. a) Nyquist and b) Bode plot of the reference and NFTO samples.

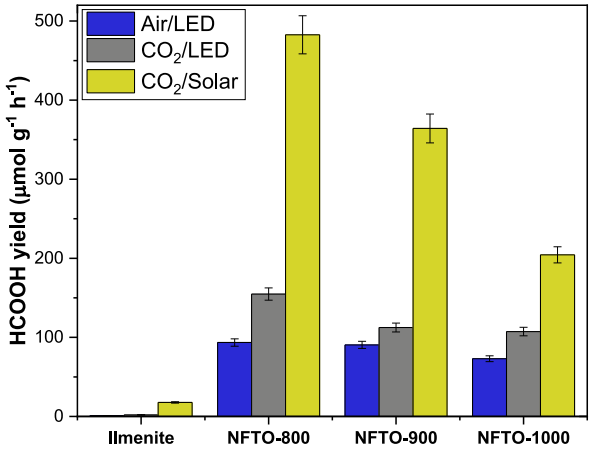

Fig. 7. Formic acid production of the reference and NFTO samples under different scenarios.

which could be related to the reduction of carbon residues on the catalyst surface [38]. On the contrary, under an argon atmosphere, the NFTO-800 sample exhibited a lower activity (<1 μmol) due to the lack of reactive carbon species to carry out its reduction to HCOOH.

4.1. Renewable process: analysis of the stability of the photocatalysts

The stability of the solar-driven CO_2 reduction using the NFTO-800 sample as a photocatalyst was evaluated on seven different days under solar light irradiation. The formic acid production is shown in Fig. 8. Since it is a solar-driven reaction, it is expected to obtain fluctuations in the activity, e.g., on days 3 and 4, the production slightly decreased, probably due to a lower solar irradiance, and thus, a decreased activation of the $NaFeTiO_4$ catalysts. After 7 days, the photocatalytic CO_2 reduction efficiency to produce formic acid maintains about 85%, demonstrating that $NaFeTiO_4$ catalysts exhibited photostability during the CO_2 reduction, which is a critical requirement for their application in other engineering levels. These results agree with recent reports that demonstrated that photocatalysts with adequate properties maintain outstanding performance with almost no decrease in CO_2 reduction [39,40].

Additionally, the morphological stability of the $NaFeTiO_4$ catalysts was investigated after the photocatalytic test. After the photocatalytic reaction, the rod-like particles still present in the NFTO-800 samples even after seven days of continuous evaluation under solar-light irradiation, as is shown in Fig. 9a and b. Also, the analysis of the EDS revealed the presence of the same elements, e.g., O, Fe, Ti, and Na, which confirmed the stability of the synthesized photocatalyst from an earth-abundant mineral.

4.2. Photocatalytic mechanism

Based on the photocatalytic activity of the NFTO-800 samples, the reaction mechanism shown in Scheme 2 was proposed for CO_2 reduction. In this process, the photocatalysts were first extracted from earth-abundant materials to obtain rod-like $NaFeTiO_4$ particles covered by Fe^{3+}/Fe^{2+} species, which influenced the photocatalytic activity obtained. In this mechanism, the $NaFeTiO_4$ photocatalyst absorbs solar light, promoting the transfer of electrons (−) from the valence (VB) to the conduction band (CB), leaving holes (+) in the first band. As a result, the photogenerated charges can migrate to the surface to react to the adsorbed species, e.g., CO_2 and H_2O, to promote the formation of HCOOH.

To corroborate that the $NaFeTiO_4$ material has the thermodynamic potential required for the CO_2 reduction to HCOOH, Mott-Schottky analysis was performed in the NFTO-800 sample (Fig. S5). According to the results, the flat band potential of the $NaFeTiO_4$ semiconductor resulted in −0.99 V *vs.* NHE, which is enough to reduce CO_2 to HCOOH, as is shown in Scheme 2. However, the presence of Fe^{3+}/Fe^{2+} species influenced the activity since this pair act as an electron scavenger, decreasing the photocatalytic activity of the material. According to previous reports, Fe^{3+} species react with the electrons to produce Fe^{2+}, which it occurs faster than the backward reaction [36]. This effect can significantly enhance the efficiency of other photocatalytic applications, e.g., oxidation reactions, to remove emerging pollutants [36,42]. However, this effect needs to be lowered for reduction reactions to obtain higher yields. Thus, the design of novel and advanced materials in the future needs to consider separating the iron species of the catalysts.

5. Conclusions

Solar-driven CO_2 reduction was demonstrated using $NaFeTiO_4$ (NFTO) photocatalyst obtained by earth-abundant minerals. The NFTO photocatalysts showed a rod-like morphology partially covered by iron oxide particles. A lower amount of Fe^{2+}/Fe^{3+} species on the rods favored higher surface area, and thus, better efficiencies for CO_2 reduction to generate HCOOH under both visible and solar-light irradiation. The stability of the $NaFeTiO_4$ catalysts was demonstrated during one week of continuous evaluation under solar light, which good results were attributed to its good morphological stability that allows the constant production of the solar fuels. These

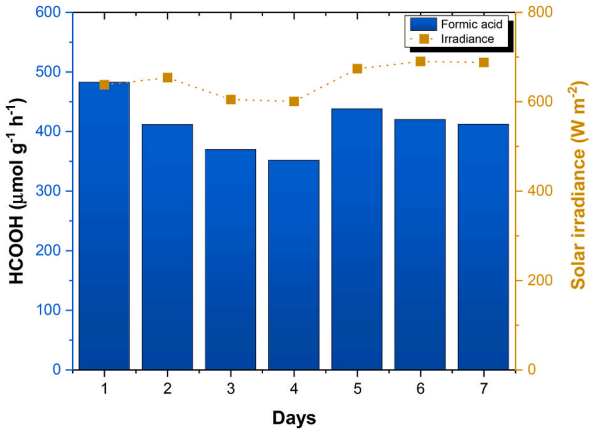

Fig. 8. Formic acid production with the NFTO-800 sample after seven days of evaluation under solar light.

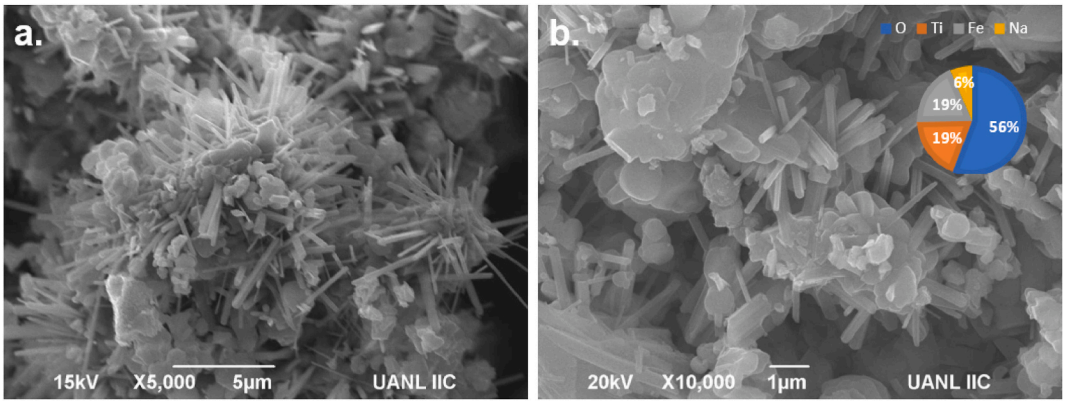

Fig. 9. SEM images of the NFTO-800 sample after the solar-driven CO_2 reduction at different magnifications a. 5000× and b. 10,000×. Input: EDS analysis of the sample.

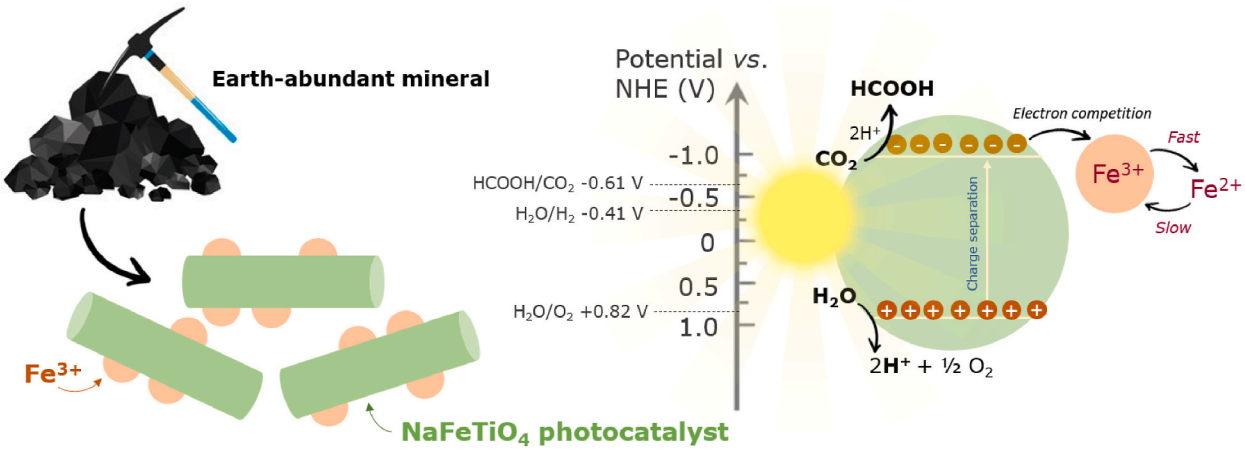

Scheme 2. Photocatalytic mechanism proposed using $NaFeTiO_4$ photocatalysts obtained from ilmenite mineral.

results confirm that it is possible to use earth-abundant minerals to synthesize highly active photocatalysts for CO_2 reduction to generate renewable solar fuels.

Author contribution statement

Edith Luévano-Hipólito: Conceived and designed the experiments; Performed the experiments; Analyzed and interpreted the data; Wrote the paper.

Mayte G. Fabela-Cedillo: Performed the experiments.

Leticia M Torres-Martínez: Conceived and designed the experiments; Wrote the paper.

María E. Zarazúa-Morín: Contributed reagents, materials, analysis tools or data.

Data availability statement

The data will be available on request.

Declaration of competing interest

The authors declare that they have no known competing financial interests or personal relationships that could have appeared to influence the work reported in this paper.

Acknowledges

The authors thank CONACYT for financial support of this research through the projects: Cátedras CONACYT 1060 and Paradigmas y Fronteras de la Ciencia 320379. Also, the authors would like to thank UANL for the support of PROVERICYT.

Appendix A. Supplementary data

Supplementary data to this article can be found online at https://doi.org/10.1016/j.heliyon.2023.e17426.

References

[1] Ž. Kovačič, B. Likozar, M. Huš, Photocatalytic CO2 reduction: a review of Ab initio mechanism, kinetics, and multiscale modeling simulations, ACS Catal. 10 (24) (2020) 14984–15007, https://doi.org/10.1021/acscatal.0c02557.

[2] E. Luévano-Hipólito, L.M. Torres-Martínez, Earth-abundant ZnS/ZnO/CuFeS2 films for air purification and solar fuels production, Mater. Sci. Semicond. Process. 134 (2021), 106029, https://doi.org/10.1016/j.mssp.2021.106029.

[3] E. Luévano-Hipólito, L.M. Torres-Martínez, Dolomite-supported Cu2O as heterogeneous photocatalysts for solar fuels production, Mater. Sci. Semicond. Process. 116 (2020), 105119, https://doi.org/10.1016/j.mssp.2020.105119.

[4] K. Kocía, V. Matejka, P. Kovár, Z. Lacny, L. Obalová, Comparison of the pure TiO2 and kaolinite/TiO2 composite as catalyst for CO2 photocatalytic reduction, Catal. Today 161 (2011) 105–109, https://doi.org/10.1016/j.cattod.2010.08.026.

[5] Y. Liu, C. Zhang, A. Shi, S. Zuo, C. Yao, C. Ni, X. Li, Full solar spectrum driven CO2 conversion over S-Scheme natural mineral nanocomposite enhanced by LSPR effect, Powder Technol. 396 (2022) 615–625, https://doi.org/10.1016/j.powtec.2021.11.024.

[6] J. Zheng, Z. Zhu, G. Gao, Z. Liu, Q. Wang, Y. Yan, Construction of spindle structured CeO2 modified with rod-like attapulgite as a high-performance photocatalyst for CO2 reduction, Catal. Sci. Technol. 9 (2019) 3788–3799, https://doi.org/10.1039/C9CY00824A.

[7] B. Tahir, M. Tahir, M.G.M. Nawawi, Well-designed 3D/2D/2D WO3/Bt/g-C3N4 Z-scheme heterojunction for tailoring photocatalytic CO2 methanation with 2D-layered bentonite-clay as the electron moderator under visible light, Energy Fuels 34 (11) (2020) 14400–14418, https://doi.org/10.1021/acs.energyfuels.0c02637.

[8] K. Ohta, Y. Ueda, S. Nakaguchi, T. Mizuno, Can. J. Chem. 76 (1998) 228–233, https://doi.org/10.1139/v97-227.

[9] T. Tao, Y. Chen, D. Zhou, H. Zhang, S. Liu, R. Amal, N. Sharma, A.M. Glushenkov, Expanding the applications of the ilmenite mineral to the preparation of nanostructures: TiO2 nanorods and their photocatalytic properties in the degradation of oxalic acid, Chem. Eur J. 19 (3) (2013) 1091–1096, https://doi.org/10.1002/chem.201202451.

[10] N.T. Truong, H.P.N. Thi, H.D. Ninh, X.T. Phung, C.V. Tran, T.T. Nguyen, T.D. Pham, T.D. Dang, S.W. Chang, E.R. Rene, H.H. Ngo, D.D. Nguyen, D.D. La, Facile fabrication of graphene@Fe-Ti binary oxide nanocomposite from ilmenite ore: an effective photocatalyst for dye degradation under visible light irradiation, J. Water Proc. Eng. 37 (2020), 101474, https://doi.org/10.1016/j.jwpe.2020.101474.

[11] L. Usgodaarachchi, C. Thambiliyagodage, R. Wijesekera, S. Vigneswaran, M. Kandanapitiye, Fabrication of TiO2 spheres and a visible light active α-Fe2O3/TiO2-rutile/TiO2-anatase heterogeneous photocatalyst from natural ilmenite, ACS Omega 7 (31) (2022) 27617–27637, https://doi.org/10.1021/acsomega.2c03262.

[12] R.B. Lee, K.M. Lee, C.W. Lai, G.-T. Pan, T.C.K. Yang, J.C. Juan, The relationship between iron and Ilmenite for photocatalyst degradation, Adv. Powder Technol. 29 (8) (2018) 1779–1786, https://doi.org/10.1016/j.apt.2018.04.013.

[13] S. Kalantari, G. Emtiazi, Comparison of ilmenite and nano-ilmenite for dye removal and antibacterial activities, Journal of Nanosciences: Curr. Res. 1 (1) (2016) 1–5, https://doi.org/10.4172/2572-0813.1000101.

[14] Q.D. Truong, J.-Y. Liu, C.-C. Chung, Y.-C. Ling, Photocatalytic reduction of CO2 on FeTiO3/TiO2 photocatalyst, Catal. Commun. 19 (2012) 85–89, https://doi.org/10.1016/j.catcom.2011.12.025.

[15] D. Sethi, N. Jada, R. Kumar, S. Ramasamy, S. Pandey, T. Das, J. Kalidoss, P.S. Mukherjee, A. Tiwari, Synthesis and characterization of titania nanorods from ilmenite for photocatalytic annihilation of E. coli, J. Photochem. Photobiol. B Biol. 140 (2014) 69–78, https://doi.org/10.1016/j.jphotobiol.2014.07.007.

[16] L. Palliyaguru, U.S. Kulathunga, L.I. Jayarathna, C.D. Jayaweera, P.M. Jayaweera, A simple and novel synthetic route to prepare anatase TiO2 nanopowders from natural ilmenite via the H3PO4/NH3 process, Int. J. Miner. Metall. Mater. 27 (2020) 846, https://doi.org/10.1007/s12613-020-2030-3.

[17] V.N. Krasil'nikov, V.P. Zhukov, L.A. Perelyaeva, I.V. Baklanova, I.R. Shein, Electronic band structure, optical absorption, and photocatalytic activity of iron doped anatase, Phys. Solid State 55 (2013) 1903–1912, https://doi.org/10.1134/S1063783413090199.
[18] C. Thambiliyagodage, R. Wijesekera, M.G. Bakker, Leaching of ilmenite to produce titanium based materials: a review, Discover Materials 1 (2021) 1, https://doi.org/10.1007/s43939-021-00020-0.
[19] Y. Liu, T. Qi, J. Chu, Q. Tong, Y. Zhang, Decomposition of ilmenite by concentrated KOH solution under atmospheric pressure, Int. J. Miner. Process. 81 (2006) 79–84, https://doi.org/10.1016/j.minpro.2006.07.003.
[20] Q. Zhao, M. Li, L. Zhou, M. Zheng, T. Zhang, Removal of metallic iron from reduced ilmenite by Aeration leaching, Metals 10 (8) (2020) 1020, https://doi.org/10.3390/met10081020.
[21] L. Palliyaguru, M.U.S. Kulathunga, K.G. Upul, R. Kumarasinghe, C.D. Jayaweera, P.M. Jayaweera, Facile synthesis of titanium phosphates from ilmenite mineral sand: potential white pigments for cosmetic applications, J. Cosmet. Sci. 70 (3) (2019) 149–159.
[22] P.V. Ananthapadmanabhan, P.R. Taylor, Titanium carbide–iron composite coatings by reactive plasma spraying of ilmenite, J. Alloys Compd. 287 (1–2) (1999) 121–125, https://doi.org/10.1016/S0925-8388(99)00061-4.
[23] D. Kang, C. Hu, Q. Zhu, Morphology controlled synthesis of hierarchical structured Fe2O3 from natural ilmenite and its high performance for dyes adsorption, Appl. Surf. Sci. 459 (2018) 327–335, https://doi.org/10.1016/j.apsusc.2018.07.220.
[24] M.A.R. Dewan, G. Zhang, O. Ostrovski, Phase development in carbothermal reduction of ilmenite concentrates and synthetic rutile, ISIJ Int. 50 (2010) 647–653, https://doi.org/10.2355/isijinternational.50.647.
[25] A. Wang, Y. Si, H. Yin, J. Chen, J. Huo, Synthesis of Na-, Fe-, and Mg-containing titanate nanocomposites starting from ilmenite and NaOH and adsorption kinetics, isotherms, and thermodynamics of Cu(II), Cd(II), and Pb(II) cations, Mater. Sci. Eng., B 249 (2019), 114411, https://doi.org/10.1016/j.mseb.2019.114411.
[26] Y. Inoue, Y. Asai, K. Sato, Photocatalysts with tunnel structures for decomposition of water, J. Chem. Soc., Faraday Trans. 90 (5) (1994) 797–802.
[27] D.S. Shinde, P.D. Bhange, S.S. Arbuj, J.-Y. Kim, J.-H. Bae, K.-W. Nam, S.N. Tayade, D.S. Bhange, NaFeTiO4: a novel visible light active photocatalyst for water splitting and environmental remediation, Int. J. Hydrogen Energy 45 (15) (2020) 8605–8617, https://doi.org/10.1016/j.ijhydene.2020.01.083.
[28] E. Ksepko, P. Babinski, L. Nalbandian, The redox reaction kinetics of Sinai ore for chemical looping combustion applications, Appl. Energy 190 (2017) 1258–1274, https://doi.org/10.1016/j.apenergy.2017.01.026.
[29] B. Mandal, A.K. Thakur, Evaluation of NaFeTiO4 as an electrode for energy storage application, Ionics 24 (2018) 1065–1074, https://doi.org/10.1007/s11581-017-2281-9.
[30] H. Zhang, M. Li, Z. Zhou, L. Shen, N. Bao, Microstructure and morphology control of potassium magnesium titanates and sodium iron titanates by molten salt synthesis, Materials 12 (10) (2019) 1577, https://doi.org/10.3390/ma12101577.
[31] Y. Zhang, W. Liu, C. Wu, T. Gong, J. Wei, M. Ma, K. Wang, M. Zhong, D. Wu, Photoluminescence of Fe2O3 nanoparticles prepared by laser oxidation of Fe catalysts in carbon nanotubes, Mater. Res. Bull. 43 (2008) 3490–3494.
[32] S.S. Pedro, O. Nakamura, R.B. Barthem, L.P. Sosman, Photoluminescence and photoacoustic spectroscopies of Fe3+ in the LiGa5O8–LiGaSiO4–Li5GaSi2O8 system, J. Fluorescence 19 (2009) 211–219, https://doi.org/10.1007/s10895-008-0404-4.
[33] K.S. Merija, K.M. Rahulan, R.A. Sujatha, N.A.L. Flower, Adsorption of hexavalent chromium from water using graphene oxide/zinc molybdate nanocomposite: study of kinetics and adsorption isotherms, Front. Energy Res. 11 (2023) 1–10, https://doi.org/10.3389/fenrg.2023.1139604.
[34] L.R. López, P. Dessì, A. Cabrera-Codony, L. Rocha-elogno, B. Kraakman, V. Naddeo, M.D. Balaguer, S. Puig, CO2 in indoor environments: from environmental and health risk to potential renewable carbon source, Sci. Total Environ. 856 (2023), 159088, https://doi.org/10.1016/j.scitotenv.2022.159088.
[35] O. Kéri, E. Kocsis, D.A. Karajz, Z.K. Nagy, B. Parditka, Z. Erdélyi, A. Szabó, K. Hernádi, I.M. Szilágyi, Photocatalytic crystalline and amorphous TiO2 nanotubes prepared by electrospinning and Atomic layer deposition, Molecules 26 (19) (2021) 5917, https://doi.org/10.3390/molecules26195917.
[36] X. Huang, J. Zhao, X. Xiong, S. Liu, Y. Xu, Positive effect of Fe3+ ions on Bi2WO6, Bi2MoO6 and BiVO4 photocatalysis for phenol oxidation under visible light, Catal. Sci. Technol. 9 (2019) 4413–4421, https://doi.org/10.1039/C9CY00855A.
[37] Studies on CO2 adsorption and desorption properties from various types of iron oxides (FeO, Fe2O3, and Fe3O4), A Hakim, TS marliza, NMA tahari, RWNW isahak, RM Yusop, WMM Hisham, AM Yarmo, Ind. Eng. Chem. Res. 55 (2016) 7888–7897, https://doi.org/10.1021/acs.iecr.5b04091.
[38] Artificial photosynthesis over crystalline TiO2-based catalysts: fact or fiction? in: C.-C. Yang, Y.-H. Yu, B. van der Linden, J.C.S. Wu, G. Mul (Eds.), J. Am. Chem. Soc. 132 (2010) 8398–8406, https://doi.org/10.1021/ja101318k.
[39] J. Jiang, X. Wang, Q. Xu, Z. Mei, L. Duan, H. Guo, Understanding dual-vacancy heterojunction for boosting photocatalytic CO2 reduction with highly selective conversion to CH4, Appl. Catal. B Environ. 316 (2022), 121679, https://doi.org/10.1016/j.apcatb.2022.121679.
[40] X. Wang, J. Jiang, Q. Xu, L. Duan, H. Guo, Understanding inclusive quantum dots hollow CN@CIZS heterojunction for enhanced photocatalytic CO2 reduction, Appl. Surf. Sci. 604 (2022), 154601, https://doi.org/10.1016/j.apsusc.2022.154601.
[42] D. Komaraiah, E. Radha, J. Sivakumar, M.V. Ramana Reddy, R. Sayanna, Influence of Fe3+ ion doping on the luminescence emission behavior and photocatalytic activity of Fe3+, Eu3+-codoped TiO2 thin films, J. Alloys Compd. 868 (2021), 159109, https://doi.org/10.1016/j.jallcom.2021.159109.